On the Impact of Hardware Impairments on RIS-aided Localization

Cüneyd Öztürk*, Musa Furkan Keskin†, Henk Wymeersch†, Sinan Gezici*
*Department of Electrical and Electronics Engineering, Bilkent University, Turkey
†Department of Electrical Engineering, Chalmers University of Technology, Sweden

Abstract—We investigate a reconfigurable intelligent surface (RIS)-aided near-field localization system with single-antenna user equipment (UE) and base station (BS) under hardware impairments by considering a practical phase-dependent RIS amplitude variations model. To analyze the localization performance under the mismatch between the practical model and the ideal model with unit-amplitude RIS elements, we employ the misspecified Cramér-Rao bound (MCRB). Based on the MCRB derivation, the lower bound (LB) on the mean-squared error for estimation of UE position is evaluated and shown to converge to the MCRB at low signal-to-noise ratios (SNRs). Simulation results indicate more severe performance degradation due to the model misspecification with increasing SNR. In addition, the mismatched maximum likelihood (MML) estimator is derived and found to be tight to the LB in the high SNR regime. Finally, we observe that the model mismatch can lead to an order-of-magnitude localization performance loss at high SNRs.

Index Terms—Localization, intelligent surfaces, hardware impairments.

I. INTRODUCTION

Among the envisioned technological enablers for 6G, three stand out as being truly disruptive: the transition from 30 GHz to beyond 100 GHz (the so-called higher mmWave and lower THz bands) [1]–[3], the convergence of communication, localization, and sensing (referred to as integrated sensing and communication (ISAC) or integrated sensing, localization, and communication (ISLAC)) [4]–[8], and the introduction of reconfigurable intelligent surfaces (RISs) [9]–[11]. RISs are large passive surfaces, comprising arrays of metamaterials, and have the ability to shape the propagation environment, thus locally boosting the signal-to-noise ratio (SNR) to improve communication quality [12], [13]. This is especially relevant in beyond 100 GHz to overcome sudden drops in rate caused by temporary blockage of the line-of-sight (LoS) path.

In parallel with the benefits for communications, RISs can similarly improve localization performance [14]. Stronger even, RISs with known position and orientation have the ability to enable localization in scenarios where it would otherwise be impossible [15]. In this respect, the large aperture of the RIS has several interesting properties. First of all, the SNR-boosting provides accurate delay measurements when wideband signals are used [2], [16]. Secondly, the large number of elements provides high resolution in angle-of-arrival (AoA) (for uplink localization) or angle-of-departure (AoD) (for downlink localization) [2]. Third, when the user equipment (UE) is close to the RIS (in the sense that the distance to the RIS is of similar order as the physical size of the RIS), wavefront curvature effects (so-called geometric near-field) can be harnessed to localize the user [14], [17]–[19], even when the LoS path between the base station (BS)
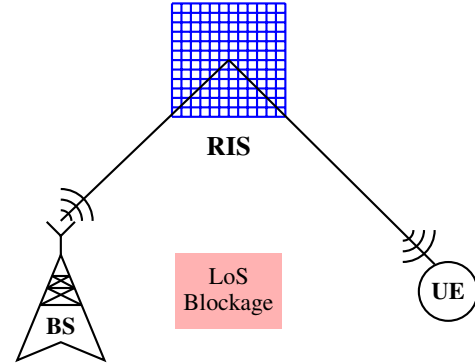

Fig. 1. Configuration of a RIS-aided localization system with LoS blockage.

and UE is blocked, irrespective of whether wideband or narrowband signals are used. Critical to the use of RIS is the control of the RIS elements, commonly through phase shifters. These phase shifters provide element-by-element control with a certain resolution, and allow the designer to coherently add up paths to or from the RIS [13], [20]. For localization, in contrast to communication, the receiver should know the values of the RIS phase profiles to apply suitable high-accuracy processing methods [11]. The ability to modulate the RIS phase profiles has additional benefits, such as separating the controlled and uncontrolled multipath through temporal coding [21]. Hence, the ability to control in a precise and known manner is essential for ISLAC applications, which necessitates the availability of accurate and simple RIS phase control models. Such models should ideally account for the per-element response [22], the finite quantization of the control [13], [23], mutual coupling [24], calibration effects, as well as power losses. Most studies on RIS localization have considered ideal phase shifters (e.g. [15]–[17], [19], [25]), ignoring the listed impairments. How these proposed localization studies fare under these impairments is both unknown and important.

In this paper, we study the impact of realistic RIS control models [22] in a geometric near-field scenario with LoS blockage and a single-antenna UE and BS. In particular, we employ the misspecified Cramér-Rao bound (MCRB) [26] as a tool to assess the loss of localization performance under model mismatch, where the algorithm assumes an ideal phase control model, different from the real phase control [22]. Our contributions are as follows: *(i)* we provide a simple expression to find the pseudo-true parameter for the considered scenario; *(ii)* we derive the MCRB of the pseudo-true parameter and the lower bound (LB) of the true parameter;

(iii) we evaluate the MCRB and LB and compare with the mismatched maximum likelihood (MML) estimator, showing that at high SNR, the model mismatch can lead to an order-of-magnitude localization performance degradation, both in terms of the LB and the matching MML. In contrast, when the true phase control model is available, localization performance is relatively stable, for all considered model parameter settings.

II. SYSTEM MODEL

In this section, we describe the system geometry, present the signal model and the RIS phase shift model, and formulate the problem of interest.

A. Geometry and Signal Model

We consider a RIS-aided localization system (see Fig. 1) with a single-antenna BS, an M-element RIS, and a single-antenna UE having the following three-dimensional locations: p_{BS} denotes the known BS location, $p_{\mathrm{RIS}} = [\mathrm{x_R}\,\mathrm{y_R}\,\mathrm{z_R}]^\mathsf{T}$ is the known center of the RIS, $p_m = [\mathrm{x}_m\,\mathrm{y}_m\,\mathrm{z}_m]^\mathsf{T}$ represents the known location of the mth RIS element for $1 \le m \le M$, and $\bar{p} = [\mathrm{x_{UE}}\,\mathrm{y_{UE}}\,\mathrm{z_{UE}}]^\mathsf{T}$ is the unknown UE location.

Without loss of generality, the BS broadcasts a narrow-band signal s_t over T transmissions under the constraint of $\mathbb{E}\{|s_t|^2\} = E_s$. Assuming LoS blockage and the absence of uncontrolled multipath, the signal received by the UE involves only reflections from the RIS and can be expressed at transmission t as

$$y_t = \bar{\alpha}\underbrace{a^\mathsf{T}(\bar{p})\mathrm{diag}(w_t)a(p_{\mathrm{BS}})}_{\triangleq b^\mathsf{T}(\bar{p})w_t}s_t + n_t, \qquad (1)$$

where $\bar{\alpha}$ is the unknown channel gain, $w_t = [w_{t,1}\,\ldots\,w_{t,M}]^\mathsf{T}$ is the RIS phase profile at transmission t, and n_t is uncorrelated zero-mean additive Gaussian noise with variance $N_0/2$ per real dimension. Moreover, $b(\bar{p}) = a(\bar{p}) \odot a(p_{\mathrm{BS}})$, where $a(p)$ is the near-field RIS steering vector for a given position p, defined as $[a(p)]_m = \exp(-j2\pi(\|p - p_m\| - \|p - p_{\mathrm{RIS}}\|)/\lambda)$, for $m \in \{1,\ldots,M\}$, in which λ denotes the signal wavelength.

B. RIS Phase Shift Model

Following the practical phase shift model in [22], we consider *phase-dependent amplitude variations* of the RIS elements, given by

$$w_{t,m} = \beta(\theta_{t,m})e^{j\theta_{t,m}}, \qquad (2)$$

with $\theta_{t,m} \in [-\pi,\pi)$ and $\beta(\theta_{t,m}) \in [0,1]$ denoting the phase shift and the corresponding amplitude, respectively. In particular, $\beta(\theta_{t,m})$ is expressed as

$$\beta(\theta_{t,m}) = (1 - \beta_{\min})\left(\frac{\sin(\theta_{t,m} - \phi) + 1}{2}\right)^\kappa + \beta_{\min}, \quad (3)$$

where $\beta_{\min} \ge 0$, $\phi \ge 0$, and $\kappa \ge 0$ are the constants related to the specific circuit implementation [22].

C. Problem Description

Given the observations in y_t from (1) over T transmission instances, our goal is to derive theoretical performance bounds for estimating the position of the UE under mismatch between the *true model* in (2) and *the assumed model* with $\tilde{w}_{t,m} =$ $\exp(j\theta_{t,m})$ (which is equivalent to assuming $\beta_{\min} = 1$). In other words, we aim to quantify localization performance loss due to this model mismatch resulting from the RIS hardware impairment specified in (2). To that end, we will resort to the MCRB analysis [26]–[29], as discussed in the next section.

III. MISSPECIFIED CRAMÉR-RAO BOUND ANALYSIS

In this section, we introduce several notations and definitions, including the MCRB and LB, before deriving the MCRB for our scenario.

A. Preliminaries

The likelihood functions under the true and assumed models are given, respectively, by

$$p(y|\eta) = \frac{1}{(\pi N_0)^T}e^{-\frac{1}{N_0}\|y - \mu(\eta)\|^2}, \qquad (4)$$

$$\tilde{p}(y|\eta) = \frac{1}{(\pi N_0)^T}e^{-\frac{1}{N_0}\|y - \tilde{\mu}(\eta)\|^2}, \qquad (5)$$

where $y \triangleq [y_1\,\ldots\,y_T]^\mathsf{T}$, $\mu(\eta) \triangleq [\mu_1(\eta)\,\ldots\,\mu_T(\eta)]^\mathsf{T}$, and $\tilde{\mu}(\eta) \triangleq [\tilde{\mu}_1(\eta)\,\ldots\,\tilde{\mu}_T(\eta)]^\mathsf{T}$. Also, the noise-free observations under the true and assumed models are

$$\mu_t(\eta) \triangleq \alpha\sum_{m=1}^{M}[b(p)]_m w_{t,m}s_t, \qquad (6)$$

$$\tilde{\mu}_t(\eta) \triangleq \alpha\sum_{m=1}^{M}[b(p)]_m \tilde{w}_{t,m}s_t, \qquad (7)$$

where $w_{t,m}$ is defined in (2), while under the assumed model $\tilde{w}_{t,m} = \exp(j\theta_{t,m})$.

B. MCRB Definition

We first introduce the pseudo-true parameter

$$\eta_0 = \arg\min_{\eta\in\mathbb{R}^5} D\left(p(y|\bar{\eta})\|\tilde{p}(y|\eta)\right), \qquad (8)$$

where $D\left(p(y|\bar{\eta})\|\tilde{p}(y|\eta)\right)$ denotes the Kullback-Leibler (KL) divergence between the distributions $p(y|\bar{\eta})$ and $\tilde{p}(y|\eta)$. Next, let $\hat{\eta}(y)$ be a misspecified-unbiased (MS-unbiased) estimator of $\bar{\eta}$, i.e., the mean of the estimator $\hat{\eta}(y)$ under the true model is equal to η_0. Then, the MCRB is a lower bound for the covariance matrix of any MS-unbiased estimator of $\bar{\eta}$, $\hat{\eta}(y)$ [26], [27], [30]:

$$\mathbb{E}_p\{(\hat{\eta}(y) - \eta_0)(\hat{\eta}(y) - \eta_0)^\mathsf{T}\} \succeq \mathrm{MCRB}(\eta_0), \qquad (9)$$

where $\mathbb{E}_p\{\cdot\}$ denotes the expectation operator under the true model $p(y|\bar{\eta})$ and

$$\mathrm{MCRB}(\eta_0) \triangleq A_{\eta_0}^{-1}B_{\eta_0}A_{\eta_0}^{-1}, \qquad (10)$$

in which the (i,j)-th elements of the matrices A_{η_0} and B_{η_0} are calculated as

$$[A_{\eta_0}]_{ij} = \mathbb{E}_p\left\{\left.\frac{\partial^2}{\partial\eta_i\partial\eta_j}\ln\tilde{p}(y|\eta)\right|_{\eta=\eta_0}\right\}, \qquad (11)$$

$$[B_{\eta_0}]_{ij} = \mathbb{E}_p\left\{\left.\frac{\partial}{\partial\eta_i}\ln\tilde{p}(y|\eta)\frac{\partial}{\partial\eta_j}\ln\tilde{p}(y|\eta)\right|_{\eta=\eta_0}\right\}, \quad (12)$$

for $1 \le i, j \le 5$, with η_i denoting the ith element of η. Note that without model mismatch, $A_{\eta_0} = A_{\bar{\eta}} = -B_{\eta_0} = -B_{\bar{\eta}}$

so that the MCRB reverts to the classical Cramér-Rao bound (CRB) [27].

Since the value of the pseudo-true parameter is generally not of interest, the MCRB is used to establish the LB of any MS-unbiased estimator with respect to the true parameter value [26]

$$\mathbb{E}_p\{(\hat{\boldsymbol{\eta}}(\boldsymbol{y}) - \bar{\boldsymbol{\eta}})(\hat{\boldsymbol{\eta}}(\boldsymbol{y}) - \bar{\boldsymbol{\eta}})^\mathsf{T}\} \succeq \mathrm{LB}(\boldsymbol{\eta}_0), \qquad (13)$$

where $\mathrm{LB}(\boldsymbol{\eta}_0) \triangleq \mathrm{MCRB}(\boldsymbol{\eta}_0) + (\bar{\boldsymbol{\eta}} - \boldsymbol{\eta}_0)(\bar{\boldsymbol{\eta}} - \boldsymbol{\eta}_0)^\mathsf{T}$. The last term is a bias term; that is, $\mathrm{Bias}(\boldsymbol{\eta}_0) \triangleq (\bar{\boldsymbol{\eta}} - \boldsymbol{\eta}_0)(\bar{\boldsymbol{\eta}} - \boldsymbol{\eta}_0)^\mathsf{T}$, and it is independent of the SNR. Hence, as the SNR tends to infinity, the MCRB term goes to zero, and the bias term becomes a tight bound for the MSE of any MS-unbiased estimator.

C. MCRB Derivation for RIS-aided Localization

1) Determining the Pseudo-True Parameter: To derive the MCRB for estimating the UE position under mismatch between the amplitude models for the RIS elements, we should first calculate the $\boldsymbol{\eta}_0$ parameter in (8) for the system model described in Section II; that is, we should find the value of $\boldsymbol{\eta}$ that minimizes the KL divergence between $p(\boldsymbol{y}|\bar{\boldsymbol{\eta}})$ in (4) and $\tilde{p}(\boldsymbol{y}|\boldsymbol{\eta})$ in (5). The following lemma characterizes $\boldsymbol{\eta}_0$ for the considered system model.

Lemma 1. *The value of $\boldsymbol{\eta}$ that minimizes the KL divergence between $p(\boldsymbol{y}|\bar{\boldsymbol{\eta}})$ in (4) and $\tilde{p}(\boldsymbol{y}|\boldsymbol{\eta})$, which is a parameterized version of (5), can be expressed as*

$$\boldsymbol{\eta}_0 = \arg\min_{\boldsymbol{\eta}\in\mathbb{R}^5} \|\boldsymbol{\mu}(\bar{\boldsymbol{\eta}}) - \tilde{\boldsymbol{\mu}}(\boldsymbol{\eta})\|. \qquad (14)$$

Proof. See Appendix A. □

Hence, the pseudo-true parameter minimizes the Euclidean distance between the noise-free observation under the true and assumed models, with respect to the assumed model.

Let $\gamma(\boldsymbol{\eta}) \triangleq \|\boldsymbol{\mu}(\bar{\boldsymbol{\eta}}) - \tilde{\boldsymbol{\mu}}(\boldsymbol{\eta})\|$. It is noted from (6) and (7) that $\gamma(\boldsymbol{\eta})$ is non-convex with respect to $\boldsymbol{\eta}$; hence, it is challenging to solve (14) in its current form. Based on (5) and (7), we can re-write (14) as

$$(\boldsymbol{\alpha}_0, \boldsymbol{p}_0) = \arg\min_{(\boldsymbol{\alpha}, \boldsymbol{p})} \|\boldsymbol{\mu}(\bar{\boldsymbol{\eta}}) - \alpha\, \boldsymbol{c}(\boldsymbol{p})\|, \qquad (15)$$

where $[\boldsymbol{c}(\boldsymbol{p})]_t \triangleq \sum_{m=1}^M [\boldsymbol{b}(\boldsymbol{p})]_m \tilde{w}_{t,m} s_t$. The optimal complex-valued α for any given $\boldsymbol{p}$ can be expressed as

$$\alpha = \frac{\boldsymbol{c}^\mathsf{H}(\boldsymbol{p})\boldsymbol{\mu}(\bar{\boldsymbol{\eta}})}{\boldsymbol{c}^\mathsf{H}(\boldsymbol{p})\boldsymbol{c}(\boldsymbol{p})}. \qquad (16)$$

Inserting (16) into (15), the minimization problem can be reduced to a three-dimensional search as follows:

$$\boldsymbol{p}_0 = \arg\max_{\boldsymbol{p}} \boldsymbol{\mu}(\bar{\boldsymbol{\eta}})^\mathsf{H} \boldsymbol{\Pi}_{\boldsymbol{c}(\boldsymbol{p})} \boldsymbol{\mu}(\bar{\boldsymbol{\eta}}) , \qquad (17)$$

where $\boldsymbol{\Pi}_{\mathbf{x}} \triangleq \mathbf{x}\mathbf{x}^\mathsf{H}/\mathbf{x}^\mathsf{H}\mathbf{x}$. Therefore, $\boldsymbol{\eta}_0 = [\boldsymbol{\alpha}_0^\mathsf{T}\ \boldsymbol{p}_0^\mathsf{T}]^\mathsf{T}$ can be found by first performing a three-dimensional optimization as in (17), and then calculating α_0 via (16) and obtaining $\boldsymbol{\alpha}_0$ as $\boldsymbol{\alpha}_0 = [\mathrm{Re}(\alpha_0)\ \mathrm{Im}(\alpha_0)]^\mathsf{T}$.

Remark 1. Note that to determine the pseudo-true parameter, the true parameter (including the location $\bar{\boldsymbol{p}}$) is known; hence, it can be used to initialize the optimization problem (17), significantly reducing the computational complexity.

2) Deriving the MCRB: After finding $\boldsymbol{\eta}_0$, we compute the matrices $\boldsymbol{A}_{\boldsymbol{\eta}_0}$ from (11) and $\boldsymbol{B}_{\boldsymbol{\eta}_0}$ from (12) for evaluating the MCRB in (9). Due to page limitation, details of computation of $\boldsymbol{A}_{\boldsymbol{\eta}_0}$ and $\boldsymbol{B}_{\boldsymbol{\eta}_0}$ are not presented in this manuscript. Based on the pdf expressions in (4)–(5), (11) becomes, with $\boldsymbol{\epsilon}(\bar{\boldsymbol{\eta}}) = \boldsymbol{\mu}(\bar{\boldsymbol{\eta}}) - \tilde{\boldsymbol{\mu}}(\boldsymbol{\eta})$

$$[\boldsymbol{A}_{\boldsymbol{\eta}_0}]_{ij} = \int p(\boldsymbol{y}|\bar{\boldsymbol{\eta}}) \frac{\partial^2}{\partial \eta_i \partial \eta_j} \ln \tilde{p}(\boldsymbol{y}|\boldsymbol{\eta})\Big|_{\boldsymbol{\eta}=\boldsymbol{\eta}_0} \mathrm{d}\boldsymbol{y} \qquad (18)$$

$$= \frac{2}{N_0} \Re \left\{ \boldsymbol{\epsilon}(\bar{\boldsymbol{\eta}})^\mathsf{H} \frac{\partial^2 \tilde{\boldsymbol{\mu}}(\boldsymbol{\eta})}{\partial \eta_i \partial \eta_j} - \left(\frac{\partial \tilde{\boldsymbol{\mu}}(\boldsymbol{\eta})}{\partial \eta_i}\right)^\mathsf{H} \frac{\partial \tilde{\boldsymbol{\mu}}(\boldsymbol{\eta})}{\partial \eta_j} \right\}\Big|_{\boldsymbol{\eta}=\boldsymbol{\eta}_0}, \qquad (19)$$

where $\frac{\partial^2 \tilde{\boldsymbol{\mu}}(\boldsymbol{\eta})}{\partial \eta_i \partial \eta_j} \triangleq \left[\frac{\partial^2 \tilde{\mu}_1(\boldsymbol{\eta})}{\partial \eta_i \partial \eta_j} \cdots \frac{\partial^2 \tilde{\mu}_T(\boldsymbol{\eta})}{\partial \eta_i \partial \eta_j}\right]^\mathsf{T}$. Similarly, after some algebraic manipulation, the (i, j)th entry of matrix $\boldsymbol{B}_{\boldsymbol{\eta}_0}$ in (12) can be written as

$$[\boldsymbol{B}_{\boldsymbol{\eta}_0}]_{ij} = \frac{2}{N_0} \left[\frac{2}{N_0} \Re \left\{ \boldsymbol{\epsilon}(\bar{\boldsymbol{\eta}})^\mathsf{H} \frac{\partial \tilde{\boldsymbol{\mu}}(\bar{\boldsymbol{\eta}})}{\partial \eta_i} \right\} \Re \left\{ \boldsymbol{\epsilon}(\bar{\boldsymbol{\eta}})^\mathsf{H} \frac{\partial \tilde{\boldsymbol{\mu}}(\bar{\boldsymbol{\eta}})}{\partial \eta_j} \right\} \right.$$
$$\left. + \Re \left\{ \left(\frac{\partial \tilde{\boldsymbol{\mu}}(\bar{\boldsymbol{\eta}})}{\partial \eta_i}\right)^\mathsf{H} \frac{\partial \tilde{\boldsymbol{\mu}}(\bar{\boldsymbol{\eta}})}{\partial \eta_j} \right\} \right]\Big|_{\boldsymbol{\eta}=\boldsymbol{\eta}_0}. \qquad (20)$$

Therefore, once we have computed the first and the second derivatives of $\tilde{\mu}_t(\boldsymbol{\eta})$ with respect to $\boldsymbol{\eta}$, we can easily compute the matrices $\boldsymbol{A}_{\boldsymbol{\eta}_0}$ and $\boldsymbol{B}_{\boldsymbol{\eta}_0}$ as specified above. The derivatives are presented in Appendix B. Based on $\boldsymbol{A}_{\boldsymbol{\eta}_0}$ and $\boldsymbol{B}_{\boldsymbol{\eta}_0}$, the MCRB in (9) and the lower bound in (13) can be evaluated in a straightforward manner.

IV. MISMATCHED ESTIMATOR

A. Definition and Relation to MCRB

We introduce the MML estimator as [26]

$$\hat{\boldsymbol{\eta}}_{\mathrm{MML}}(\boldsymbol{y}) = \arg\max_{\boldsymbol{\eta}\in\mathbb{R}^5} \ln \tilde{p}(\boldsymbol{y}|\boldsymbol{\eta}). \qquad (21)$$

Under some regularity conditions, it is shown that $\hat{\boldsymbol{\eta}}_{\mathrm{MML}}(\boldsymbol{y})$ is asymptotically MS-unbiased and its error covariance matrix is asymptotically equal to the $\mathrm{MCRB}(\boldsymbol{\eta}_0)$ [26, Thm. 2]. Hence, the covariance matrix of the MML estimator is asymptotically tight to the MCRB.

B. MML Estimator for UE Location

We now investigate the MML estimator for the UE position under model misspecification regarding the RIS amplitudes. From (5) and (21), the MML estimator based on the received signal $\boldsymbol{y}$ can be expressed as $\hat{\boldsymbol{\eta}}_{\mathrm{MML}}(\boldsymbol{y}) = \arg\min_{\boldsymbol{\eta}\in\mathbb{R}^5} \|\boldsymbol{y} - \tilde{\boldsymbol{\mu}}(\boldsymbol{\eta})\|$. Since this problem is in the same form as the optimization problem in (14), it can be reduced to a three-dimensional optimization problem as discussed in Section III-C. In order to solve the resulting problem, initialization can be very critical as we are facing with a non-convex optimization problem. During the estimation process, we do not have access to the true position $\bar{\boldsymbol{p}}$. Hence, we cannot use the true position vector $\bar{\boldsymbol{p}}$ for the initialization. If an arbitrarily chosen position vector is used for the initialization, the global optimal solution of (21) is not always

obtained. To find a remedy for this issue, we use the Jacobi-Anger expansion approach discussed in [17] to obtain an initial position vector rather than starting from an arbitrarily generated position vector. In particular, for the position vector $\bar{\boldsymbol{p}} = \|\bar{\boldsymbol{p}}\| \, [\sin(\vartheta)\cos(\varphi) \, \sin(\vartheta)\sin(\varphi) \, \cos(\vartheta)]^{\mathsf{T}}$, for some $N \in \mathbb{N}$, $\boldsymbol{a}(\bar{\boldsymbol{p}})$ is approximated as

$$[\boldsymbol{a}(\bar{\boldsymbol{p}})]_m \approx \sum_{n=-N}^{N} j^n J_n \left(-\frac{2\pi}{\lambda} \|\boldsymbol{p}_m\| \sin(\vartheta) \right) e^{jn(\varphi - \psi_m)}, \tag{22}$$

where $\boldsymbol{p}_m = \|\boldsymbol{p}_m\| \, [\cos(\psi_m) \, \sin(\psi_m) \, 0]^{\mathsf{T}}$ and $J_n(\cdot)$ is the nth order Bessel function of the first kind. After defining $\boldsymbol{G}(\varphi)$ and $\boldsymbol{h}(\varphi)$ exactly as in [17], we can rewrite y_t as

$$y_t \approx \bar{\alpha} \boldsymbol{h}^{\mathsf{T}}(\varphi) \boldsymbol{G}(\vartheta) \mathrm{diag}(\boldsymbol{w}_t) \boldsymbol{a}(\boldsymbol{p}_{\mathrm{BS}}) s_t + n_t, \tag{23}$$

By using two-step simple line searches given in [17, Eqs. 31, 32], estimates of φ and ϑ are obtained. Let $\hat{\vartheta}$ and $\hat{\varphi}$ denote the estimates of ϑ and φ. After these two steps, we generate random variables $\tilde{d}$ such that $\tilde{d}[\sin(\hat{\vartheta})\cos(\hat{\varphi}) \, \sin(\hat{\vartheta})\sin(\hat{\varphi}) \, \cos(\hat{\vartheta})]^{\mathsf{T}}$ are initial position vectors for any $\tilde{d}$. As discussed in [17], this two-step simple line searches have a low computational complexity and do not add any complexity cost to the MML estimator.

V. NUMERICAL RESULTS

In this section, we first present numerical examples for evaluating the lower bounds in various scenarios, and then compare the performance of the MML estimator against the lower bounds.

A. Simulation Setup

We consider an RIS with $M = 2500$ elements, where the inter-element spacing is $\lambda/2$ and the area of each element is $A = \lambda^2/4$ [17]. The carrier frequency is equal to $f_c = 28$ GHz. The RIS is modeled to lie in the X-Y plane with $\boldsymbol{p}_{\mathrm{RIS}} = [0\,0\,0]^{\mathsf{T}}$. Moreover, for the phase profile, the $\theta_{t,m}$ values are generated uniformly and independently between $-\pi$ and π. For the model of the RIS in (3), $\kappa = 2$ and $\phi = 0$. The BS is located at $\boldsymbol{p}_{\mathrm{BS}} = 5.77 \times [-1\,1\,1]^{\mathsf{T}}$ meters. For given distance d to the RIS, the UE is located at $d \times [1\,1\,1]^{\mathsf{T}}/\|[1\,1\,1]\|$ meters. We set the number of transmission to $T = 50$. For simplicity, we assume that $s_t = \sqrt{E_s}$ for any t. The SNR is defined as

$$\mathrm{SNR} = \frac{E_s \|\bar{\boldsymbol{\alpha}}\|^2}{T N_0} \sum_{t=1}^{T} |\boldsymbol{b}^{\mathsf{T}}(\bar{\boldsymbol{p}}) \boldsymbol{w}_t|^2 . \tag{24}$$

B. Analysis of Lower Bounds and MML Estimator

To solve (17) for LB computation, we employ the GlobalSearch algorithm of MATLAB by providing 10 different initial points. These initial points are generated by multiplying each component of the true position of the UE, $\bar{\boldsymbol{p}}$, by independent uniform random variables between zero and one.

For the initialization of the MML estimator, N in (22) is taken as 5 for using the Jacobi-Anger expansion approach. Let $\hat{\vartheta}$ and $\hat{\varphi}$ denote the estimates of ϑ and φ. After obtaining the the estimates of ϑ and φ, for the norm of the $\bar{\boldsymbol{p}}$, we generate a random variable $\tilde{d}$, between 0 and 1000 for 10 different seeds, and we run the GlobalSearch algorithm of MATLAB for each initial point.
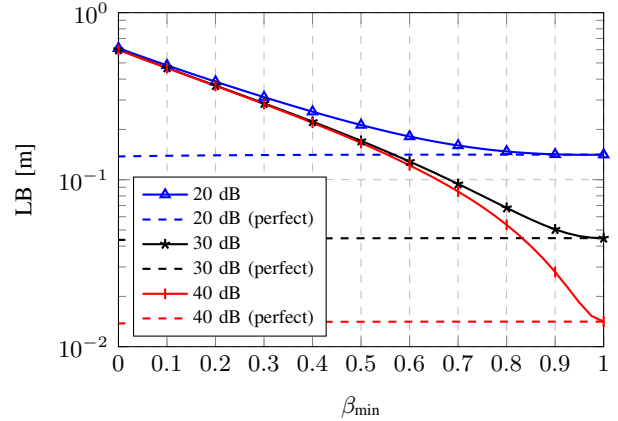

Fig. 2. LB versus $\beta_{\min}$ for SNR = 20 dB, 30 dB and 40 dB when the UE distance is 5 meters. The curves marked (perfect) are nearly flat and correspond to the the assumed model being equal to the true model for different $\beta_{\min}$.

C. Results and Discussion

In Fig. 2, we show LB as a function of $\beta_{\min}$ for SNRs of 20, 30, and 40 dB when the UE distance is 5 meters from the center of the RIS. In addition, for comparison purposes, the lower bounds in the presence of the perfect knowledge of the $\beta_{\min}$ values are also presented (marked as "Perfect" in the figure).[1] We observe from the figure that as $\beta_{\min}$ decreases, i.e., as the mismatch between the true and the assumed models increases, the LB increases and raising the SNR level does not improve the LB values significantly. In addition, the sensitivity to the model mismatch is more pronounced at higher SNR, while for an SNR of 20 dB, the performance is relatively insensitive for $\beta_{\min} > 0.7$. Interestingly, we note that when the true model is known (i.e., in the presence of perfect knowledge of $\beta_{\min}$), the value of $\beta_{\min}$ does not influence the LB values notably.

In Fig. 3, to understand the impact of the number of RIS elements, by averaging 200 different random phase profiles, average LB values versus RIS size are shown at an SNR of 30 dB. We consider $\beta_{\min} \in \{0.3, 0.5, 0.7\}$. Moreover, the average lower bounds under the perfect knowledge of the $\beta_{\min}$ values are plotted. We observe that as the RIS size increases or as $\beta_{\min}$ increases, we obtain lower LB values in general. Interestingly, the curves for different $\beta_{\min}$ values are almost parallel. We note the significant price we pay under mismatch: with perfect knowledge of a RIS with 1000 elements attains similar performance as a RIS with 7000 elements when $\beta_{\min} = 0.5$ under mismatch.

Finally, in Fig. 4, we show the performance of the MML estimator versus SNR for $\beta_{\min} = 0.3$ and 0.7 when the UE distance is 5 meters. In addition to the performance of the MML estimator, the LB, and the MCRB, the bias term values are also plotted. We observe that the MML estimator exhibits three distinct regimes: a low-SNR regime where MML is

---

[1]To obtain these curves, it is assumed that for any given $\beta_{\min}$, the perfect knowledge of the RIS amplitudes is available. Hence, this bound reduces to the classical CRB expression as in [17, Eq. 9]. As $\boldsymbol{\mu}$ changes with respect to the true value of $\beta_{\min}$, this expression is computed for each $\beta_{\min}$ value.
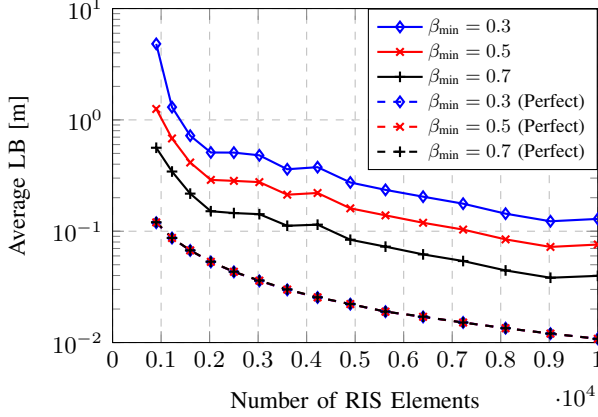
Fig. 3. Average LB versus RIS size for $\beta_{\min} \in \{0.3, 0.5, 0.7\}$, when SNR = 30 dB, and the UE distance is 5 meters.
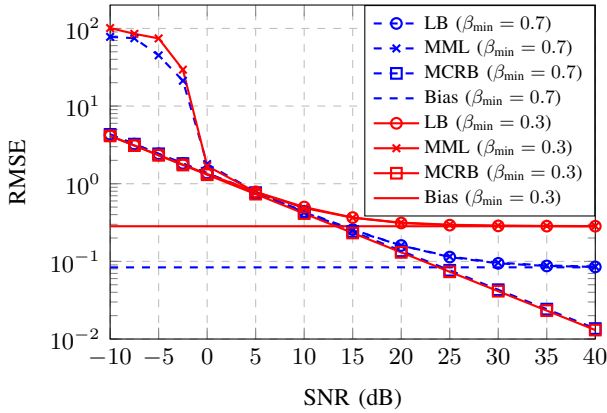

Fig. 4. MML, LB, MCRB, and bias term versus SNR (dB) for $\beta_{\min} \in \{0.3, 0.7\}$ when the UE distance is 5 meters.

limited by noise peaks and thus far away from the LB; a medium-SNR regime where MML is close to the LB, which itself is dominated by the MCRB; and a high-SNR regime, where the MML and LB are limited by the bias term Bias($\boldsymbol{\eta}_0$).

VI. Concluding Remarks

We have considered the problem of RIS-aided near-field localization in the presence of model misspecification accounting for mismatch between ideal and realistic RIS amplitude models. In particular, we have focused on a scenario in which the exact model for the amplitudes of the RIS elements is unknown and the amplitudes are assumed to be constant (unity). Based on the realistic amplitude model given in [22], we have first derived the theoretical performance bounds for estimating the UE position when the belief and the reality of the RIS amplitude models do not match. We have observed that the amplitude knowledge becomes crucial in the high SNR regime. Moreover, when the true model is known, the value of $\beta_{\min}$ does not affect the theoretical bounds notably. Lastly, we have implemented the MML estimator for the considered problem, and observed that the MML estimator can achieve the LB in the high-SNR regime, as expected.

Appendix A
Proof of Lemma 1

Based on the definition of the KL divergence and the system model in Section II, (8) can be expressed as

$$\boldsymbol{\eta}_0 = \arg\min_{\boldsymbol{\eta} \in \mathbb{R}^5} \int p(\boldsymbol{y}|\bar{\boldsymbol{\eta}}) \ln\left(\frac{p(\boldsymbol{y}|\bar{\boldsymbol{\eta}})}{\tilde{p}(\boldsymbol{y}|\boldsymbol{\eta})}\right) \mathrm{d}\boldsymbol{y} \qquad (25)$$

$$= \arg\min_{\boldsymbol{\eta} \in \mathbb{R}^5} - \int p(\boldsymbol{y}|\bar{\boldsymbol{\eta}}) \ln \tilde{p}(\boldsymbol{y}|\boldsymbol{\eta}) \mathrm{d}\boldsymbol{y} \qquad (26)$$

$$= \arg\min_{\boldsymbol{\eta} \in \mathbb{R}^5} \int p(\boldsymbol{y}|\bar{\boldsymbol{\eta}}) \|\boldsymbol{y} - \tilde{\boldsymbol{\mu}}(\boldsymbol{\eta})\|^2 \mathrm{d}\boldsymbol{y} \qquad (27)$$

where the second equality is due to the independence of $p(\boldsymbol{y} \mid \bar{\boldsymbol{\eta}})$ from $\boldsymbol{\eta}$, and the last equality is obtained from (5). Then, it can be shown that the following equations hold:

$$\int p(\boldsymbol{y}|\bar{\boldsymbol{\eta}}) \|\boldsymbol{y} - \tilde{\boldsymbol{\mu}}(\boldsymbol{\eta})\|^2 \, d\boldsymbol{y} = \sum_{t=1}^{T} \int p(\boldsymbol{y}|\bar{\boldsymbol{\eta}}) |y_t - \tilde{\mu}_t(\boldsymbol{\eta})|^2 \, d\boldsymbol{y}$$

$$= \sum_{t=1}^{T} \underbrace{\left(\prod_{t' \neq t} \int p(y_{t'}|\bar{\boldsymbol{\eta}}) \, dy_{t'}\right)}_{=1} \left(\int p(y_t|\bar{\boldsymbol{\eta}}) |y_t - \tilde{\mu}_t(\boldsymbol{\eta})|^2 \, dy_t\right)$$

$$= \sum_{t=1}^{T} \int p(y_t|\bar{\boldsymbol{\eta}}) |y_t - \tilde{\mu}_t(\boldsymbol{\eta})|^2 \, dy_t. \qquad (28)$$

We now introduce $\epsilon_t(\boldsymbol{\eta}) = \mu_t(\bar{\boldsymbol{\eta}}) - \tilde{\mu}_t(\boldsymbol{\eta})$, so that $|y_t - \tilde{\mu}_t(\boldsymbol{\eta})|^2 = |y_t - \mu_t(\bar{\boldsymbol{\eta}}) + \epsilon_t(\boldsymbol{\eta})|^2$, and the integral expression in (28) can be manipulated as follows:

$$\int p(y_t|\bar{\boldsymbol{\eta}}) |y_t - \tilde{\mu}_t(\boldsymbol{\eta})|^2 \, dy_t$$

$$= \int p(y_t|\bar{\boldsymbol{\eta}}) |y_t - \mu_t(\bar{\boldsymbol{\eta}})|^2 \, dy_t + |\epsilon_t(\boldsymbol{\eta})|^2 \int p(y_t|\bar{\boldsymbol{\eta}}) \, dy_t$$

$$+ 2 \int p(y_t|\bar{\boldsymbol{\eta}}) \Re\left((y_t - \mu_t(\bar{\boldsymbol{\eta}}))^* \epsilon_t(\boldsymbol{\eta})\right) \, dy_t. \qquad (29)$$

Since $y_t \sim \mathcal{CN}(\mu_t(\bar{\boldsymbol{\eta}}), N_0)$ and $\int p(y_t|\bar{\boldsymbol{\eta}}) \, dy_t = 1$, the expression in (29) can be simplified as

$$\int p(y_t|\bar{\boldsymbol{\eta}}) |y_t - \tilde{\mu}_t(\boldsymbol{\eta})|^2 \, dy_t = N_0 + |\epsilon_t(\boldsymbol{\eta})|^2. \qquad (30)$$

By combining (27), (28) and (30), we finally obtain that

$$\bar{\boldsymbol{\eta}} = \arg\min_{\boldsymbol{\eta} \in \mathbb{R}^5} \sum_{t=1}^{T} \left(N_0 + |\epsilon_t(\boldsymbol{\eta})|^2\right) = \arg\min_{\boldsymbol{\eta} \in \mathbb{R}^5} \sum_{t=1}^{T} |\epsilon_t(\boldsymbol{\eta})|^2,$$

which completes the proof.

Appendix B
Derivation of Entries in the MCRB

Let $\boldsymbol{\eta}$ be given by $\boldsymbol{\eta} = [\alpha_r \, \alpha_i \, \mathrm{x} \, \mathrm{y} \, \mathrm{z}]^\mathsf{T}$. Also, define $\boldsymbol{p} \triangleq [\mathrm{x} \, \mathrm{y} \, \mathrm{z}]^\mathsf{T}$, $b_m \triangleq [\boldsymbol{b}(\boldsymbol{p})]_m$, and $\alpha \triangleq \alpha_r + j\alpha_i$. We also introduce $\boldsymbol{u} = \frac{\boldsymbol{p} - \boldsymbol{p}_{\mathrm{RIS}}}{\|\boldsymbol{p} - \boldsymbol{p}_{\mathrm{RIS}}\|}$ and for any $1 \leq m \leq M$, $\boldsymbol{u}_m = \frac{\boldsymbol{p} - \boldsymbol{p}_m}{\|\boldsymbol{p} - \boldsymbol{p}_m\|}$, where

$\boldsymbol{u} = [u_x\, u_y\, u_z]^\mathsf{T}$ and $\boldsymbol{u}_m = [u_{m,x}\, u_{m,y}\, u_{m,z}]^\mathsf{T}$. Then, the first and second derivatives of $\tilde{\mu}_t(\boldsymbol{\eta})$ with respect to $\boldsymbol{\eta}$ are given as follows:

$$\frac{\partial \tilde{\mu}_t(\boldsymbol{\eta})}{\partial \alpha_r} = \sum_{m=1}^{M} b_m \tilde{w}_{t,m} s_t, \quad \frac{\partial \tilde{\mu}_t(\boldsymbol{\eta})}{\partial \alpha_i} = j \sum_{m=1}^{M} b_m \tilde{w}_{t,m} s_t.$$

For $\nu \in \{x\, y\, z\}$, we can write

$$\frac{\partial \tilde{\mu}_t(\boldsymbol{\eta})}{\partial \nu} = -j \frac{2\pi}{\lambda} \alpha \sum_{m=1}^{M} b_m \left(u_{m,\nu} - u_x\right) \tilde{w}_{t,m} s_t,$$

$$\frac{\partial^2 \tilde{\mu}_t(\boldsymbol{\eta})}{\partial \alpha_r \partial \nu} = -j \frac{2\pi}{\lambda} \sum_{m=1}^{M} b_m \left(u_{m,\nu} - u_\nu\right) \tilde{w}_{t,m} s_t,$$

$$\frac{\partial^2 \tilde{\mu}_t(\boldsymbol{\eta})}{\partial \alpha_i \partial \nu} = j \frac{\partial^2 \tilde{\mu}_t(\boldsymbol{\eta})}{\partial \alpha_r \partial \nu},$$

$$\frac{\partial^2 \tilde{\mu}_t(\boldsymbol{\eta})}{\partial \nu \partial \nu} = -\alpha \frac{4\pi^2}{\lambda^2} \sum_{m=1}^{M} b_m \left(u_{m,\nu} - u_\nu\right)^2 \tilde{w}_{t,m} s_t$$
$$- j \frac{2\pi}{\lambda} \alpha \sum_{m=1}^{M} b_m \left(\frac{1 - u_{m,\nu}^2}{\|\boldsymbol{p} - \boldsymbol{p}_m\|} - \frac{1 - u_\nu^2}{\|\boldsymbol{p} - \boldsymbol{p}_{\mathrm{RIS}}\|} \right) \tilde{w}_{t,m} s_t.$$

Moreover, if $\nu_1, \nu_2 \in \{x\, y\, z\}$ and they correspond to different coordinates, it is possible express that

$$\frac{\partial^2 \tilde{\mu}_t(\boldsymbol{\eta})}{\partial \nu_1 \partial \nu_2} = -\alpha \frac{4\pi^2}{\lambda^2} \sum_{m=1}^{M} b_m \left(u_{m,\nu_1} - u_{\nu_1}\right) \left(u_{m,\nu_2} - u_{\nu_2}\right) \tilde{w}_{t,m} s_t$$
$$+ j \frac{2\pi}{\lambda} \alpha \sum_{m=1}^{M} b_m \left(\frac{u_{m,\nu_1} u_{m,\nu_2}}{\|\boldsymbol{p} - \boldsymbol{p}_m\|} - \frac{u_{\nu_1} u_{\nu_2}}{\|\boldsymbol{p} - \boldsymbol{p}_{\mathrm{RIS}}\|} \right) \tilde{w}_{t,m} s_t.$$

REFERENCES

[1] W. Saad *et al.*, "A vision of 6G wireless systems: Applications, trends, technologies, and open research problems," *IEEE Network*, vol. 34, no. 3, pp. 134–142, 2019.
[2] T. S. Rappaport *et al.*, "Wireless Communications and Applications Above 100 GHz: Opportunities and Challenges for 6G and Beyond," *IEEE Access*, vol. 7, pp. 78 729–78 757, 2019.
[3] H. Tataria *et al.*, "6G Wireless Systems: Vision, Requirements, Challenges, Insights, and Opportunities," *Proc. IEEE*, vol. 109, no. 7, pp. 1166–1199, 2021.
[4] A. R. Chiriyath *et al.*, "Radar-communications convergence: Coexistence, cooperation, and co-design," *IEEE Trans. Cogn. Commun. Netw.*, vol. 3, no. 1, pp. 1–12, 2017.
[5] F. Liu *et al.*, "Integrated Sensing and Communications: Towards Dual-functional Wireless Networks for 6G and Beyond," 2021. [Online]. Available: https://arxiv.org/abs/2108.07165
[6] C. De Lima *et al.*, "Convergent Communication, Sensing and Localization in 6G Systems: An Overview of Technologies, Opportunities and Challenges," *IEEE Access*, vol. 9, pp. 26 902–26 925, 2021.
[7] H. Wymeersch *et al.*, "Integration of Communication and Sensing in 6G: a Joint Industrial and Academic Perspective," 2021. [Online]. Available: https://arxiv.org/abs/2106.13023
[8] D. K. Pin Tan *et al.*, "Integrated Sensing and Communication in 6G: Motivations, Use Cases, Requirements, Challenges and Future Directions," in *IEEE Int. Online Symposium on Joint Commun. and Sensing (JCS)*, 2021, pp. 1–6.
[9] Q. Wu *et al.*, "Intelligent Reflecting Surface-Aided Wireless Communications: A Tutorial," *IEEE Trans. Commun.*, vol. 69, no. 5, pp. 3313–3351, 2021.
[10] A. Elzanaty *et al.*, "Towards 6G Holographic Localization: Enabling Technologies and Perspectives," 2021. [Online]. Available: https://arxiv.org/abs/2103.12415
[11] H. Wymeersch *et al.*, "Radio Localization and Mapping With Reconfigurable Intelligent Surfaces: Challenges, Opportunities, and Research Directions," *IEEE Veh. Technol. Mag.*, vol. 15, no. 4, pp. 52–61, 2020.
[12] E. Basar *et al.*, "Wireless Communications Through Reconfigurable Intelligent Surfaces," *IEEE Access*, vol. 7, pp. 116 753–116 773, 2019.
[13] C. Pan *et al.*, "Reconfigurable Intelligent Surfaces for 6G Systems: Principles, Applications, and Research Directions," *IEEE Commun. Mag.*, vol. 59, no. 6, pp. 14–20, 2021.
[14] S. Hu *et al.*, "Beyond Massive MIMO: The Potential of Positioning With Large Intelligent Surfaces," *IEEE Trans. Signal Process.*, vol. 66, no. 7, pp. 1761–1774, 2018.
[15] K. Keykhosravi *et al.*, "SISO RIS-Enabled Joint 3D Downlink Localization and Synchronization," in *IEEE Int. Conf. Commun.*, 2021, pp. 1–6.
[16] A. Elzanaty *et al.*, "Reconfigurable Intelligent Surfaces for Localization: Position and Orientation Error Bounds," *IEEE Trans. Signal Process.*, pp. 1–1, 2021.
[17] Z. Abu-Shaban *et al.*, "Near-field Localization with a Reconfigurable Intelligent Surface Acting as Lens," in *IEEE Int. Conf. Commun.*, 2021, pp. 1–6.
[18] F. Guidi *et al.*, "Radio Positioning With EM Processing of the Spherical Wavefront," *IEEE Trans. Wireless Commun.*, vol. 20, no. 6, pp. 3571–3586, 2021.
[19] M. Rahal *et al.*, "RIS-Enabled Localization Continuity Under Near-Field Conditions," 2021. [Online]. Available: https://arxiv.org/abs/2109.11965
[20] H. Guo *et al.*, "Weighted Sum-Rate Maximization for Reconfigurable Intelligent Surface Aided Wireless Networks," *IEEE Trans. Wireless Commun.*, vol. 19, no. 5, pp. 3064–3076, 2020.
[21] K. Keykhosravi *et al.*, "Multi-RIS Discrete-Phase Encoding for Interpath-Interference-Free Channel Estimation," 2021. [Online]. Available: https://arxiv.org/abs/2106.07065
[22] S. Abeywickrama *et al.*, "Intelligent Reflecting Surface: Practical Phase Shift Model and Beamforming Optimization," *IEEE Trans. Commun.*, vol. 68, no. 9, pp. 5849–5863, 2020.
[23] P. Xu *et al.*, "Reconfigurable Intelligent Surfaces-Assisted Communications With Discrete Phase Shifts: How Many Quantization Levels Are Required to Achieve Full Diversity?" *IEEE Wireless Commun. Lett.*, vol. 10, no. 2, pp. 358–362, 2021.
[24] G. Gradoni *et al.*, "End-to-End Mutual Coupling Aware Communication Model for Reconfigurable Intelligent Surfaces: An Electromagnetic-Compliant Approach Based on Mutual Impedances," *IEEE Wireless Commun. Lett.*, vol. 10, no. 5, pp. 938–942, 2021.
[25] W. Wang *et al.*, "Joint Beam Training and Positioning for Intelligent Reflecting Surfaces Assisted Millimeter Wave Communications," *IEEE Trans. Wireless Commun.*, pp. 1–1, 2021.
[26] S. Fortunati *et al.*, "Performance Bounds for Parameter Estimation under Misspecified Models: Fundamental Findings and Applications," *IEEE Signal Process. Mag.*, vol. 34, no. 6, pp. 142–157, 2017.
[27] ——, "Chapter 4: Parameter bounds under misspecified models for adaptive radar detection," in *Academic Press Library in Signal Processing, Volume 7*, R. Chellappa *et al.*, Eds. Academic Press, 2018, pp. 197–252.
[28] T. T. Le *et al.*, "Misspecified Cramer-Rao Bounds for Blind Channel Estimation under Channel Order Misspecification," *IEEE Trans. Signal Process.*, pp. 1–1, 2021.
[29] F. Roemer, "Misspecified Cramer-Rao Bound For Delay Estimation with a Mismatched Waveform: A Case Study," in *IEEE Int. Conf. Acoustics, Speech Signal Process.*, 2020, pp. 5994–5998.
[30] C. D. Richmond *et al.*, "Parameter Bounds on Estimation Accuracy Under Model Misspecification," *IEEE Trans. Signal Process.*, vol. 63, no. 9, pp. 2263–2278, 2015.